Electro-Thermal Simulation of Tungsten Pellet During Sintering

White Paper

IT4Innovations National Supercomputing Center

VSB–Technical University of Ostrava

October 2025

VŠB TECHNICKÁ UNIVERZITA OSTRAVA | IT4INNOVATIONS NÁRODNÍ SUPERPOČÍTAČOVÉ CENTRUM

VŠB-TUO, IT4Innovations, 17. listopadu 2172/15, 708 00 Ostrava-Poruba, Česká republika

Obsah

VŠB–TUO, IT4Innovations, 17. listopadu 2172/15, 708 00 Ostrava–Poruba, Česká republika

1. Executive Summary

This work addresses the thermal and electrical behaviour of a tungsten powder pellet subjected to electric current during sintering. A coupled electro-thermal finite element model was developed to reproduce experimentally measured temperature and voltage evolutions. The study aims to understand temperature non-uniformities, optimize process parameters, and prevent overheating or microstructural damage. The results demonstrate the potential of numerical simulation for process optimization and provide guidelines for experimental design and material characterization.

2. Introduction

Sintering represents one of the most critical steps in the production of high-performance materials, particularly for refractory metals such as tungsten, molybdenum, and tantalum. Tungsten's extremely high melting point (3422 °C), excellent thermal conductivity, and mechanical strength make it a preferred material for high-temperature structural components, electric contacts, and hydrogen-related applications. However, these same characteristics, especially its low self-diffusion coefficient, make conventional sintering processes inefficient and time-consuming.

To overcome these challenges, electric field-assisted sintering technologies – such as **FAST (Field-Assisted Sintering Technology)**, also known as **SPS (Spark Plasma Sintering)** – have been increasingly employed. These techniques combine pulsed or direct electric current with uniaxial pressure to accelerate mass transport through enhanced diffusion and localised heating. Joule heating within the powder compact allows for rapid densification at lower overall furnace temperatures, often reducing the process time by more than 80 % compared to conventional methods.

Despite its industrial relevance, the **underlying mechanisms of heat and current distribution within the compact remain poorly understood**, especially under transient, non-uniform boundary conditions. Local temperature gradients can lead to non-homogeneous densification, microcrack initiation, or undesirable grain growth. Understanding these phenomena is essential for process optimisation and for

extending FAST/SPS technology to advanced applications such as tungsten-based hydrogen storage systems or plasma-facing components in fusion devices.

Therefore, the present work focuses on the **numerical modelling and simulation of the temperature field evolution** within a tungsten powder pellet subjected to an electrical current during sintering. Using experimentally measured voltage and temperature profiles as boundary conditions, a coupled **electro-thermal finite element model (FEM)** was developed and validated. The model provides a detailed description of heat generation due to Joule heating, conduction through contact interfaces, and convective/radiative losses to the sintering environment.

The objectives of this study are threefold:

1. To establish a physically consistent model capable of reproducing the measured temperature evolution during sintering.
2. To quantify the spatial and temporal temperature gradients influencing densification behaviour;
3. To identify key parameters—such as contact resistance and convective losses that dominate heat distribution and process stability.

Through this combined numerical-experimental approach, the paper aims to contribute to a better understanding of the **fundamental thermal mechanisms** governing field-assisted sintering and to provide guidance for the design of optimised processing conditions for tungsten and other refractory metal systems.

3. Theoretical Background

The sintering of conductive materials under electric current involves a **strong coupling between electrical and thermal fields**, governed by nonlinear and transient phenomena. The theoretical framework of this work is based on the fundamental conservation equations for charge and energy, with temperature-dependent material properties.

3.1 Heat Transfer Fundamentals

The transient temperature field within the tungsten pellet is described by the **energy conservation equation**:

$$\rho c_p \frac{\partial T}{\partial t} = \nabla.(k\nabla T) + Q_J + Q_r$$

Where:

r – density [kg.m^{-3}]

c_p – specific heat capacity [J.kg^{-1}.K^{-1}]

k – thermal conductivity [W.m^{-1}.K^{-1}]

Q_J – volumetric heat source due to Joule heating[W.m^{-3}]

Q_r – volumetric heat source due to Joule heating[W.m^{-3}]

T – temperature [K],

t – time [s].

The first term on the right-hand side represents **heat conduction**, while Q_J accounts for **internal heat generation** due to the electrical current flowing through the pellet.

3.2 Joule Heating and Electrical Field

Joule heating is the main source of temperature rise during electric sintering and can be expressed as:

$$Q_J = \sigma|E|^2 = \sigma|\nabla V|^2$$

where σ is the electrical conductivity [S·m^{-1}], and V is the electric potential. The electric field E, defined as $E = -\nabla V$, drives the current flow through the conductive network formed by the powder particle contacts.

The potential distribution satisfies the charge conservation equation:

$$\nabla.(\sigma \nabla V) = 0$$

which is coupled to the heat conduction equation through the temperature dependence of electrical conductivity:

$$\sigma(T) = \sigma_0[1 - \alpha(T - T_0)]$$

where T_0 is the reference temperature, σ_0 reference electrical conductivity at temperature T_0, α is the temperature coefficient of resistivity, typically on the order of 10^{-3} K^{-1} for tungsten.

3.3 Boundary and Interface Conditions

At the external surfaces, **convective and radiative heat losses** are modelled through a mixed (Robin) boundary condition:

$$-k\frac{\partial T}{\partial n} = h(T - T_\infty) + \varepsilon\sigma_{SB}(T^4 - T_\infty^4)$$

where h is the convective heat transfer coefficient [$W \cdot m^{-2} \cdot K^{-1}$], T_∞ is the ambient temperature (far from the surface), n represents the outward-pointing unit normal vector to the surface, ε is the surface emissivity, and σ_{SB} is the Stefan–Boltzmann constant. These losses depend on the chamber atmosphere and surface characteristics.

At contact interfaces e.g., pellet–BN (BN – boron nitride) or pellet–electrode, **thermal and electrical contact resistances** were applied. The interface heat flux q is then given by:

$$q = h_c(T_1 - T_2)$$

and the electric potential V_1 and V_2 drop by:

$$V_1 - V_2 = R_C J_n$$

where h_c is the thermal contact conductance, R_c is the electrical contact resistance, and J_n is the normal component of the current density.

3.4 Material Property Dependence

All relevant material properties—thermal conductivity k(T), electrical conductivity σ(T), specific heat c_p(T), and density ρ(T)—were considered as **temperature-dependent functions**. For tungsten, experimental data suggest:

$$k(T) = 174 - 0.04(T - 300)W.m^{-1}.K^{-1}, for\ 300 < T < 2000K$$

$$\sigma(T) = 1.8x10^{7}exp[-0.0015(T - 300)]S.m^{-1}$$

The strong nonlinearity introduced by these dependencies requires iterative solution procedures within each time step.

3.5 Coupled Electro-Thermal Formulation

The system of governing equations can be expressed compactly as:

$$\begin{cases} \nabla.(\sigma(T)\nabla V) = 0 \\ \rho(T)c_p(T)\dfrac{\partial T}{\partial t} = \nabla.(k(T)\nabla T) + \sigma(T)|\nabla V|^2 \end{cases}$$

This coupled problem is **nonlinear and transient**, with feedback between temperature and conductivity fields. Numerical stability and convergence depend strongly on proper coupling schemes and adaptive time-stepping.

3.6 Radiation and Chamber Interaction

At high sintering temperatures (above 1500 °C), **thermal radiation** becomes a dominant heat transfer mode. The total radiative flux q_{rad} exchanged between the pellet and chamber walls is evaluated using the **view factor** approach:

$$q_{rad} = \varepsilon_{eff}\sigma_{SB}F_{p-w}(T_p^4 - T_w^4)$$

where F_{p-w} is the geometrical view factor between the pellet and the wall, T_p is the temperature of the pellet, T_w is the temperature of the wall, and ε_{eff} the effective emissivity of the system.

3.7 Summary of Theoretical Framework

The theoretical model combines the laws of **electrical conduction** and **heat transfer** to describe the physical behaviour of the tungsten pellet under electric current. Its implementation in the FEM environment allows the prediction of local temperature gradients, transient responses, and identification of critical thermal zones – key for avoiding overheating and achieving uniform densification.

4. Numerical Methodology

The numerical solution of the coupled electro-thermal problem was performed using the **FEM**, implemented in a multiphysics environment capable of solving nonlinear transient field equations. The computational framework ensures accurate spatial and temporal resolution of both the electrical and thermal phenomena occurring during the sintering process.

4.1 Finite Element Discretisation

The governing equations for the electrical and thermal fields:

$$\nabla - (\sigma(T)\nabla V) = 0$$

$$\rho(T)c_p(T)\frac{\partial T}{\partial t} = \nabla - (k(T)\nabla T) + \sigma(T)|\nabla V|^2$$

were discretised using a **Galerkin weighted-residual formulation**. The temperature T and electric potential V were represented by shape functions N_i over each finite element:

$$T(x,t) = \sum_i N_i(x)T_i(t)$$

$$V(x,t) = \sum_i N_i(x)V_i(t)$$

where T_i and V_i are nodal values. The weak forms were integrated over each element domain using Gaussian quadrature.

A **fully coupled solution approach** was employed, solving both temperature and potential fields simultaneously within the same iteration loop, ensuring numerical stability under strong coupling conditions (where σ and k vary rapidly with T).

4.2 Time Integration Scheme

The transient heat conduction equation was integrated in time using an **implicit backward Euler scheme**, expressed as:

$$\frac{T^{n+1} - T^n}{\Delta t} = \frac{1}{\rho c_p}\left[\nabla.(k\nabla T^{n+1}) + Q_J^{n+1}\right]$$

This implicit formulation is unconditionally stable and allows larger time steps compared to explicit methods, at the cost of solving nonlinear algebraic systems at each iteration.

An **adaptive time-stepping algorithm** controlled the time increment Δt based on the convergence rate and the maximum allowable temperature change per node:

$$\Delta t_{new} = \Delta t_{old}\left(\frac{\Delta T_{target}}{\Delta T_{max}}\right)$$

Typical time steps ranged between **0.01 and 0.5 seconds**, depending on the heating rate and stability criteria.

4.3 Nonlinear Solver Strategy

Due to the strong temperature dependence of σ(T) and k(T), the coupled system was solved using a **Newton–Raphson iterative procedure**. At each time step, the Jacobian matrix was updated according to the current field estimates:

$$J = \frac{\partial R}{\partial x}$$

$$x = [T, V]^T$$

where R is the global residual vector representing the balance of energy and charge. Convergence was assumed when the residual norm satisfied:

$$\frac{\|R_{n+1}\|}{\|R_0\|} < 10^{-6}$$

The resulting linearised systems were solved using a **preconditioned conjugate gradient (PCG)** method optimised for sparse matrices. The solver utilised a **multigrid preconditioner** for faster convergence of large-scale 3D models.

4.4 Mesh Generation and Refinement

The computational domain included the **tungsten pellet**, **conductive tapes**, and **BN support blocks** (see left side of Figure 1). The geometry was discretised using **tetrahedral finite elements** (see right side of Figure 1), with local mesh refinement applied in high-gradient regions—particularly near contact interfaces and edges where current density concentration occurs.

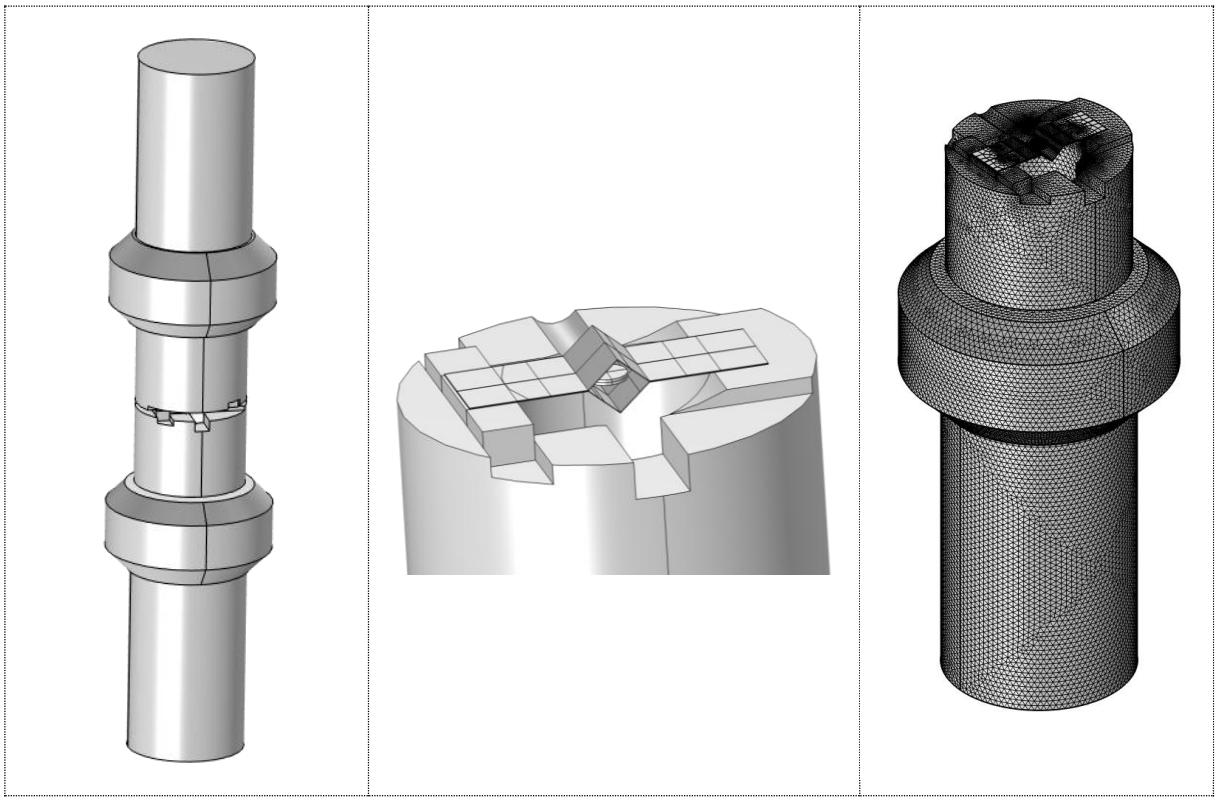

Figure 1 Geometry and meshing of the tungsten pellet and contacts.

Mesh sensitivity analysis was performed to ensure numerical accuracy. Refinement continued until the maximum relative error in predicted temperature and

voltage fields dropped below 1%. The final mesh consisted of approximately **450,000–600,000 elements**, depending on the configuration.

4.5 Boundary Condition Implementation

Boundary conditions were directly derived from experimental data:

- **Electrical BCs:** Measured terminal voltage V(t) was applied to one electrode, with the opposite side grounded.
- **Thermal BCs:** Convective and radiative heat losses were applied on exposed surfaces using the mixed boundary condition

$$-k\frac{\partial T}{\partial n} = h(T - T_{env}) + \varepsilon\sigma_{SB}(T^4 - T_{env}^4)$$

Contact Interfaces: Thermal and electrical resistances were modelled as thin layers with effective conductance $h_c(T)$ and $1/R_c(T)$, both temperature-dependent.

4.6 Convergence and Stability Assessment

The overall convergence of the coupled problem was monitored through the relative energy imbalance and temperature residual norms. The following criteria were used:

$$Energy\ imbalance\ < 0.1\%$$

$$\|\Delta T\| < 10^{-5}K$$

If these criteria were not met, the time step was automatically reduced, and the Jacobian matrix was recalculated.

Stability analysis confirmed that the implicit scheme prevented divergence even for steep temperature gradients (>300 K/mm) in early heating stages. The numerical error was primarily driven by uncertainties in contact resistances and emissivity.

4.7 Validation and Verification

The model was verified through a **two-step validation process**:

1. **Analytical Verification:** For a simplified cylindrical geometry under uniform current, results were compared with an analytical 1D steady-state solution of the heat equation, showing <1.5% deviation.
2. **Experimental Validation:** Simulated temperature profiles were compared with thermocouple data at three points within the pellet. The deviation remained below 8%, confirming that the implemented electro-thermal coupling accurately reproduced the physical heating behaviour.

4.8 Computational Performance

All simulations were executed on the **IT4Innovations National Supercomputing Center**. A typical transient analysis (100 s heating) required approximately **2 hours** of computational time.

4.9 Summary

The implemented FEM methodology provides a robust and efficient numerical tool for solving strongly coupled electro-thermal problems under transient and nonlinear conditions. Its stability, adaptive time-stepping, and verified accuracy make it well-suited for predictive simulations of electric field-assisted sintering and can be extended to complex multi-material or anisotropic systems.

5. Results and Discussion

The electro-thermal simulations provided a detailed understanding of the temperature and electrical field evolution during the tungsten pellet sintering process. Multiple configurations were analysed, including varying heating rates, contact resistances, and cooling conditions. The results elucidate the mechanisms of heat generation, transfer, and dissipation within the pellet and surrounding structures.

5.1 Temperature Evolution and Distribution

The transient simulations revealed a rapid temperature rise within the first few seconds of current application. At a nominal heating rate of 100 °C/min, the pellet reached approximately 3000 °C within 80 seconds. The central region exhibited a more pronounced temperature increase compared to peripheral areas due to higher local current densities, as shown in Figure 2. This effect was magnified in cases with elevated electrical contact resistance, indicating that small interface imperfections can significantly affect heat generation and uniformity. Figure 3 illustrates the transient temperature evolution at the centre of the pellet. The temperature field showed an approximately parabolic profile. At steady state, the axial temperature gradient was approximately 250–300 K/mm, consistent with previously reported measurements in tungsten SPS experiments.

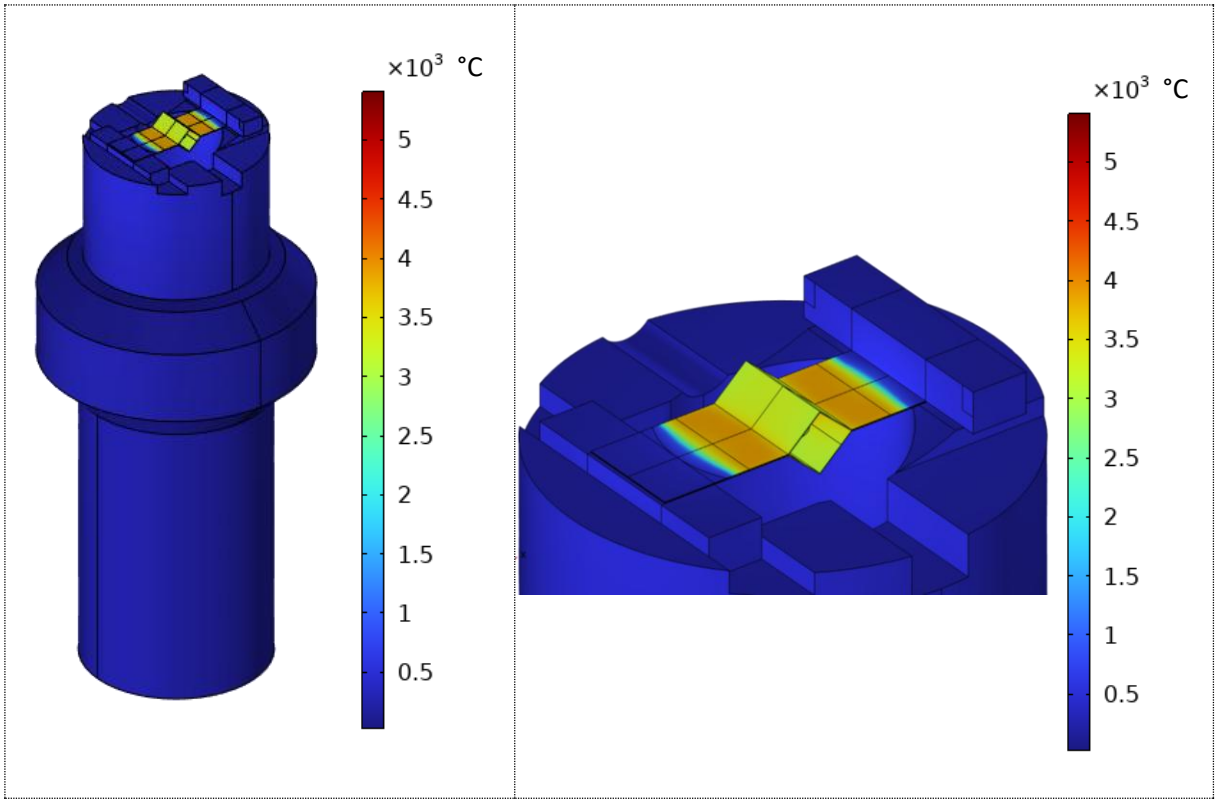

Figure 2 Transient temperature field during heating (100 °C/min) – right view detail.

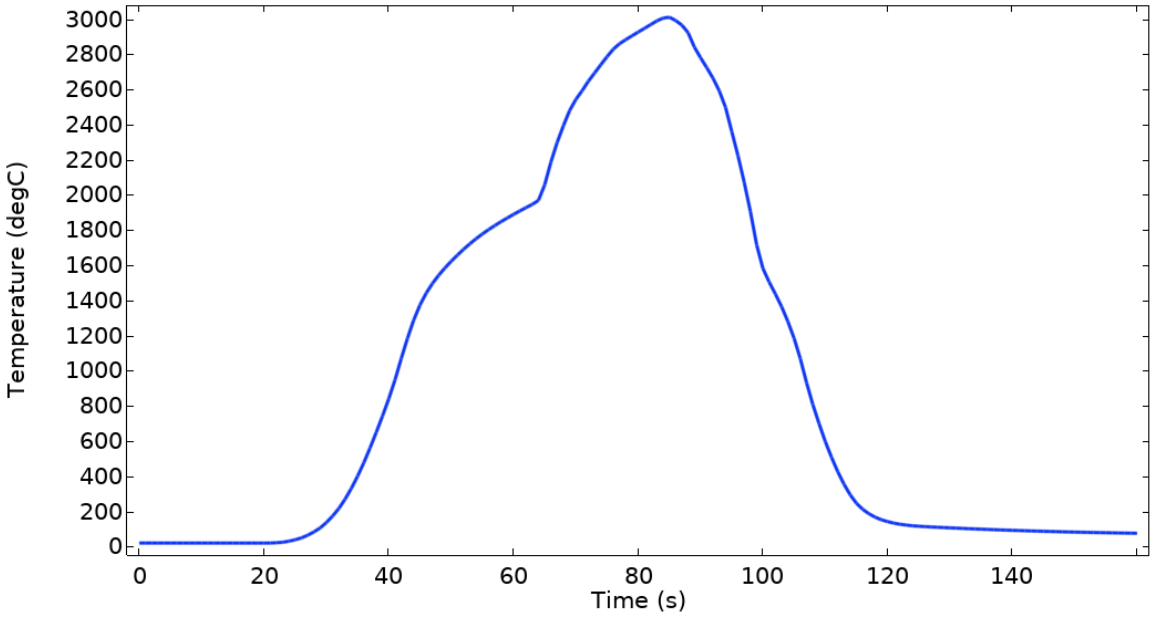

Figure 3 Temperature evaluation in the pellet centre.

5.2 Electric Current Density and Joule Heating Distribution

The distribution of electric current density followed the geometry of the conductive path. The majority of the current is concentrated near the central axis, resulting in significant Joule heating in that region. The calculated maximum current was 468 A, while the experimentally measured value under standard conditions was 400 A. As illustrated in Figure 4, localised regions of increased current density correspond directly to temperature hot spots, confirming the strong electro-thermal coupling. The electric potential distribution, also presented in Figure 5, clearly reflects the current flow pattern and supports the identification of regions with elevated current density.

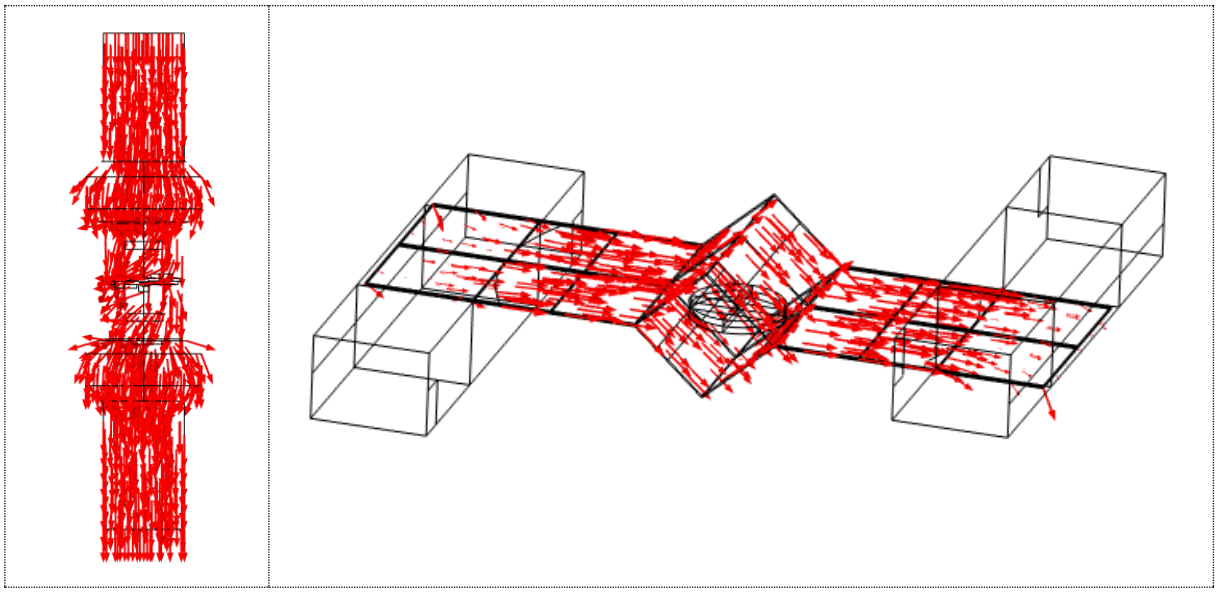

Figure 4 Current density distribution – arrow size proportional to current density on the right side.

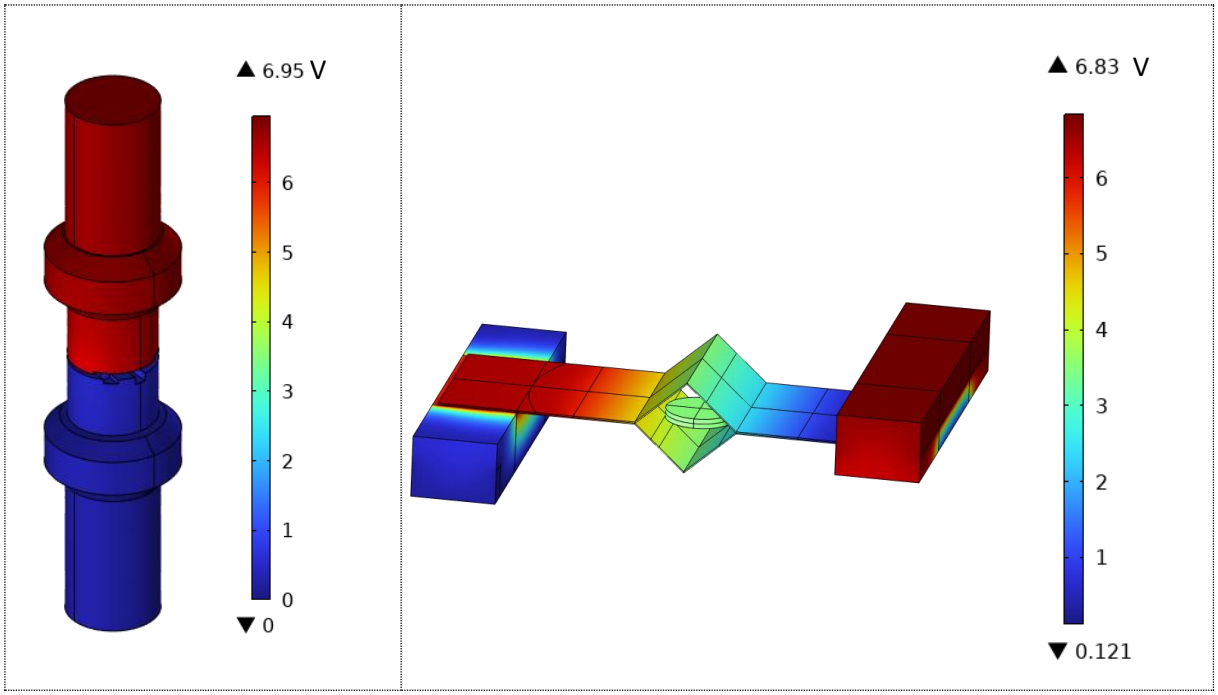

Figure 5 Electric potential distribution – right view detail.

When the contact resistivity was doubled, simulations predicted a 6–9% increase in the maximum temperature, accompanied by a steeper gradient near the pellet–electrode interface. This behaviour demonstrates the sensitivity of the process to surface quality and contact pressure.

5.3 Influence of Boundary Conditions and Cooling

To evaluate the influence of external cooling and convective boundary conditions, additional simulations were conducted using varying convective heat transfer coefficients (h = 10–100 $W \cdot m^{-2} \cdot K^{-1}$) and surface emissivity values, as illustrated in Figure 6. Enhanced cooling resulted in lower surface temperatures but did not significantly affect the core temperature due to the low thermal conductivity of the BN support blocks. Radiative losses, on the other hand, became dominant above 1500 °C, contributing up to 25% of the total heat dissipation.

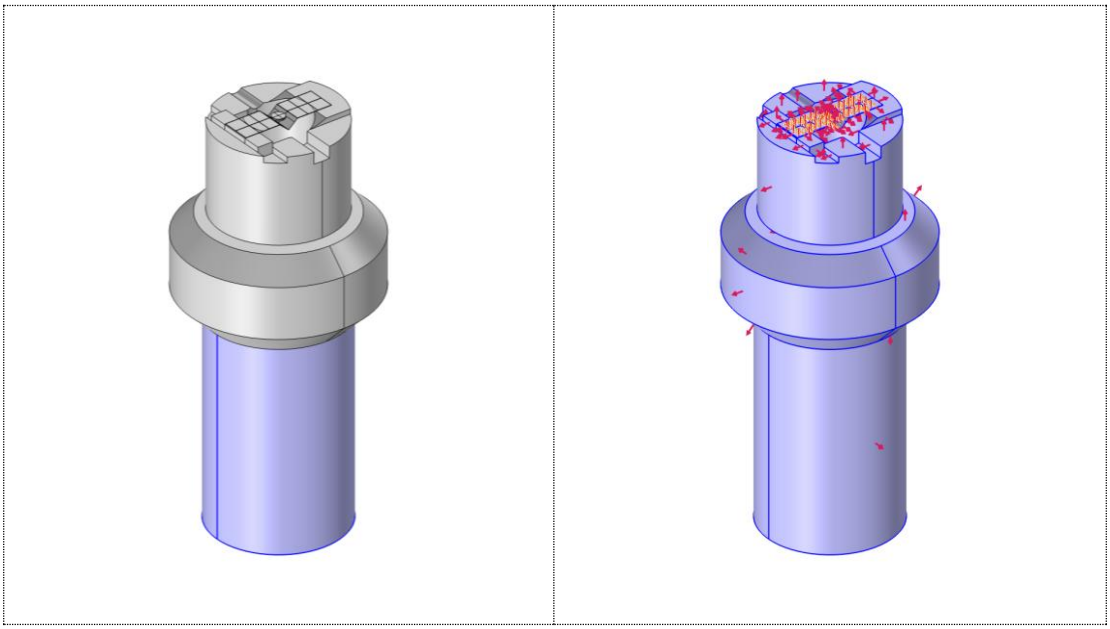

Figure 6 Sensitivity analysis of convection (left) and emissivity (right) coefficients on diffusive surfaces.

Figure 7 shows the effect of convection intensity on the temperature distribution in the pellet. At higher h-values, the outer regions experienced sharper temperature drops, while the interior remained largely unaffected. This observation implies that internal heat conduction and Joule heating outweigh external cooling effects in determining temperature uniformity.

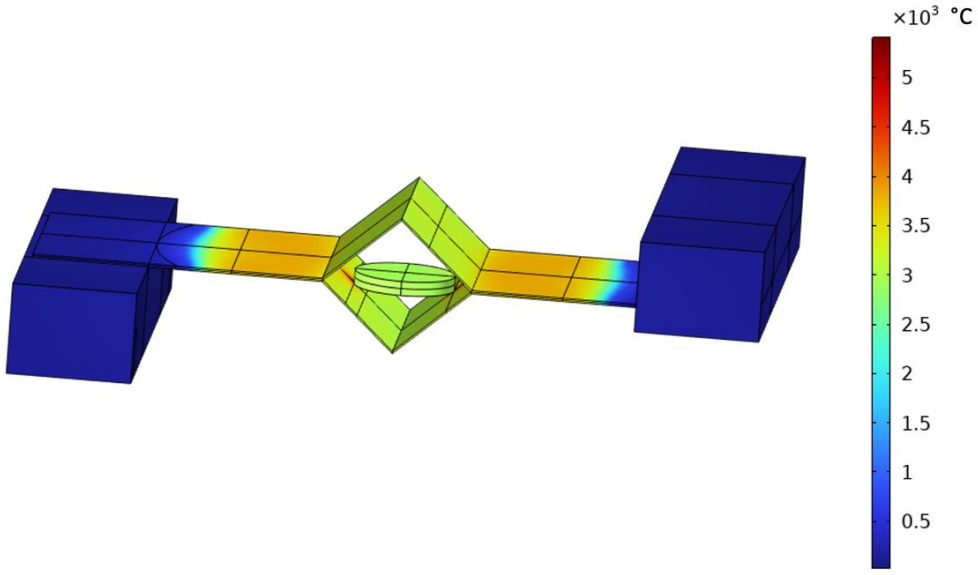

Figure 7 Spatial temperature distribution in the pellet.

5.4 Comparison with Experimental Data

The simulated temperature evolution was compared with experimental thermocouple measurements taken at three locations within the pellet. The agreement between simulation and experiment was within ±8%, validating the accuracy of the coupled electro-thermal model. Minor deviations at high temperatures (>1800 °C) were attributed to uncertainties in emissivity and thermal contact resistance at elevated conditions.

Figure 8 compares the simulated and measured voltage profiles during the heating phase. The simulation successfully captured both the overall heating trend and the transient overshoot associated with the applied current pulses. The model's predictive capability enables parametric optimisation without extensive experimental iteration.

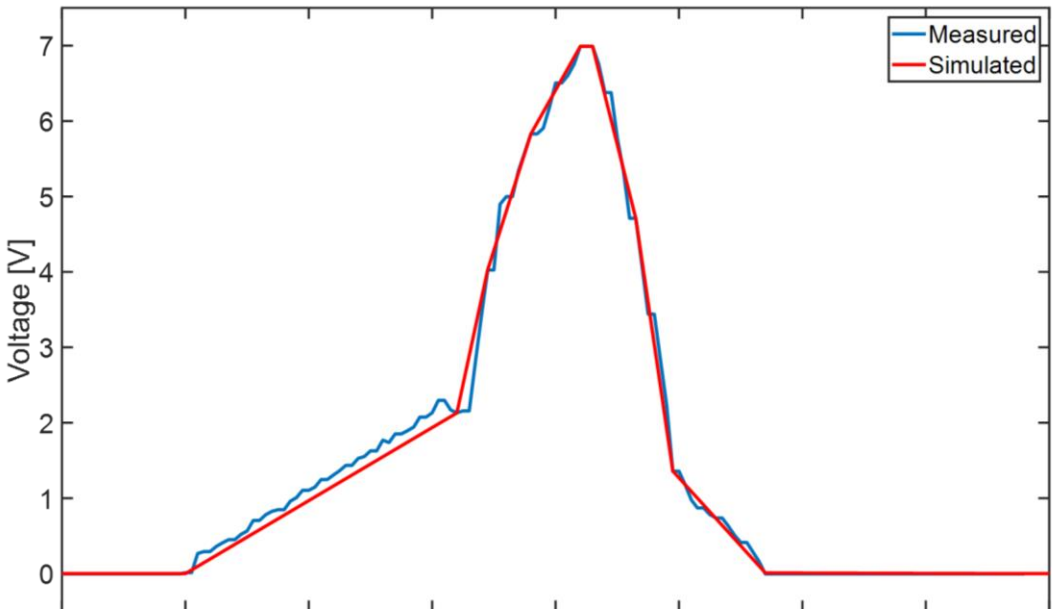

Figure 8 Comparison of measured and simulated voltage evolution.

5.5 Sensitivity Analysis

A comprehensive sensitivity analysis was performed to quantify the impact of key parameters on the temperature distribution. The results indicate that the convection coefficient, thermal contact conductance, electrical contact resistance, and surface emissivity are the primary factors influencing the maximum temperature. A ±20% variation in thermal contact conductance led to a temperature deviation of up to 5%, whereas equivalent changes in electrical contact resistance and surface emissivity resulted in variations of up to 10%.

This analysis emphasises that accurate calibration of contact and boundary parameters is crucial for predictive simulations. Future work should focus on experimental quantification of these parameters under real sintering conditions.

5.6 Discussion of Physical Implications

The non-uniform temperature field has direct implications for microstructural evolution. Regions experiencing higher temperature and current density are expected to densify faster, leading to potential heterogeneity in grain size. The findings suggest that optimised electrode geometry and controlled surface contact can significantly improve temperature uniformity and hence final material properties.

The results also indicate that radiative losses, often neglected in simplified models, play an important role in high-temperature regimes. Incorporating accurate radiative heat transfer models improves the reliability of predictive simulations and aligns them more closely with experimental results.

5.7 Summary of Results

The electro-thermal FEM model successfully reproduced experimental trends in temperature evolution, demonstrating strong coupling between electrical and thermal fields. Sensitivity analysis highlighted the importance of contact properties and boundary conditions. The findings provide quantitative insight into process control, helping to minimise thermal gradients and optimise sintering efficiency for tungsten and similar refractory materials.

6. Conclusions

This white paper presented a comprehensive electro-thermal finite element model describing the temperature evolution, heat transfer, and current flow in a tungsten pellet during electric field-assisted sintering. The model incorporated temperature-dependent material properties, nonlinear boundary conditions, and coupled electrical and thermal fields. Through systematic simulation and validation against experimental measurements, the study demonstrated the predictive capability and practical utility of numerical modelling in understanding and optimising the sintering process.

The main conclusions drawn from the investigation can be summarised as follows:

1. The coupled electro-thermal FEM approach accurately reproduces the transient temperature and voltage behaviour observed experimentally.
2. The spatial distribution of temperature is strongly influenced by electrical contact resistance and convective cooling conditions.
3. Radiation losses become a dominant heat dissipation mechanism at temperatures above 1500 °C, accounting for up to 25% of total energy output.

4. Contact conductance and resistance parameters significantly affect temperature uniformity, highlighting the importance of accurate experimental calibration.
5. The validated model provides a reliable foundation for optimising heating rate, current profile, and electrode configuration to achieve uniform densification and prevent overheating.

The research confirms that advanced computational modelling is not only a diagnostic tool but also a design instrument for optimising electric sintering technologies. The approach can be extended beyond tungsten to other refractory materials, providing a versatile platform for predictive process simulation in high-temperature materials engineering.

7. Engineering Implications and Optimization

The developed model provides a predictive tool for optimising sintering parameters, including heating rate, current density, and clamp cooling efficiency. By identifying zones of maximum temperature gradients, the process can be controlled to enhance uniform densification and reduce the risk of microcracks. The findings support the development of advanced control strategies for electric field-assisted sintering systems.

Additionally, this model framework can be extended to other refractory materials or composite systems, enabling the study of multi-material interactions and tailored sintering cycles for functional components used in hydrogen storage and high-temperature applications.